Supplement of Atmos. Chem. Phys., 22, 12401–12415, 2022
https://doi.org/10.5194/acp-22-12401-2022-supplement

Supplement of

Parameterizations of size distribution and refractive index of biomass burning organic aerosol with black carbon content

Biao Luo et al.

Correspondence to: Ye Kuang (kuangye@jnu.edu.cn) and Shan Huang (shanhuang_eci@jnu.edu.cn)

1. Methods

1.1 Determination of PMF factors from SP-AMS measurements

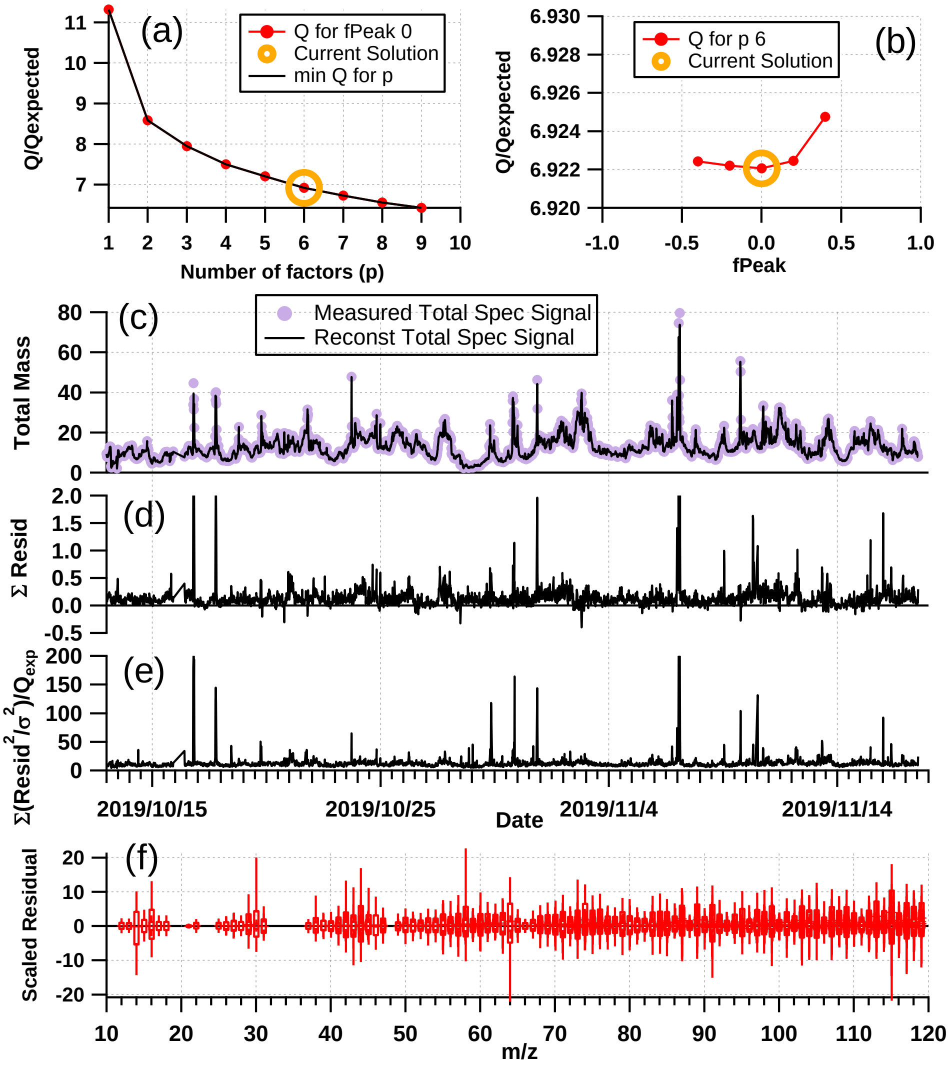

Figure S1. Diagnostics plots for PMF analysis of the SP-AMS OA mass spectra.

The source apportionment of organic aerosols (OA) was performed by positive matrix factorization (PMF) based on high resolution OA data from SP-AMS. The input data were collected in AMS V-mode using only tungsten vaporizer. PMF has been described in many other papers (Paatero, 1997; Paatero and Tapper, 1994) and has been used for AMS-based aerosol source apportionment as a common method (e.g. Huang *et al.*, 2018; Lanz *et al.*, 2007; Ng *et al.*, 2011; Sun *et al.*, 2012; Ulbrich *et al.*, 2009). In this study, high resolution AMS data including organic ion mass concentrations and their uncertainties were input to the PMF. An Igor Pro-based panel, i.e., PMF Evaluation Tool (PET, v2.06, Ulbrich et al., 2009) were used to perform PMF analysis. Before the calculation, isotopes and ions with m/z >120 were excluded to minimize the interference from repeatedly calculated uncertainties and noise signals. In total, 454 ions were considered in PMF. After investigating different solutions with factor number from 2 to 10 with fPeak varying between -1 and 1, a six-factor solution was selected based on the best performance shown by PMF quality parameters and most reasonable source identification. In the five-factor solution, two primary OA factors were mixed, while the seven and more factor solutions make factors split over. More parameters of the model performance could be found in the diagnostic plots as shown in Fig.S1.

The mass spectra, time series and diurnal variations of factors are illustrated in Fig.S2. Overall, the total OA measured in the Heshan campaign were apportioned to six sources or processes, including two primary sources : 1) a hydrocarbon-like OA (HOA, containing cooking emissions), 2) a biomass burning OA (BBOA); and four secondary sources: 3) more oxygenated OA (MOOA, regional transport), 4) less oxygenated OA (LOOA, related to daytime photochemical formation), 5) nighttime-formed OA (Night-OA), and 6) aged BBOA (aBBOA).

As the key organic aerosols in the present study, BBOA took 16.5% of the total OA mass loading. BBOA was identified by good correlation with the biomass burning emission tracer acetonitrile which measured by the parallel gaseous pollutant measurements. The correlation coefficient (R=0.60) is higher than those between other OA factors and acetonitrile. The BBOA factor was also recognized by pronounced intensity of ions $C_2H_4O_2^+$ (m/z 60.022, 0.5%) and $C_3H_5O_2^+$ (m/z 73.029, 0.4%) which were also tracers for biomass burning OA (Lanz *et al.*, 2007; Ng *et al.*, 2011). The diurnal pattern of BBOA showed a remarkable peak in the early evening (~19:00), corresponding to the local dinner period during which the people in the surrounding valleys often used biomass materials for cooking or other residential use (the smokes were observed as shown in Fig.S7). The other primary factor, HOA, was characterized by abundant hydrocarbon ions $C_xH_y^+$, such as $C_4H_7^+$ (m/z 55.055, 8.3%) and $C_4H_9^+$ (m/z 57.070, 9.5%). Because of the remarkable hydrocarbon ions and the low oxidation state (O:C =0.39), HOA was attributed to primary emissions such as vehicle exhausts; while in this study, cooking emissions cannot be fully excluded since the cooking emission tracer $C_6H_{10}O^+$ (m/z 98.073, 0.3%) was mainly distributed in the HOA factor. However, Heshan supersite is far away from the main roads and cooking is not allowed inside of the site, thus the HOA factor accounted for only 8.7% of the total OA and the diurnal variation of HOA showed no morning/evening peaks as the typical pattern of vehicle emissions at urban site. Regarding the OA factors related to the secondary processes, MOOA presented the highest oxidation state (O:C ratio = 1.0) with highest fraction of CO_2^+ (f_{CO2+} = 18%) among all factors. The negligible diurnal variation of MOOA also suggested that aerosols were probably aged during the long-range transport rather than local formed via photo-oxidation. In contrast, LOOA was recognized as local formed secondary OA via photochemical process, traced by prominent ion $C_2H_3O^+$ (m/z 43.018, 10.3%) and clear afternoon-peak in the diurnal pattern. With a similar

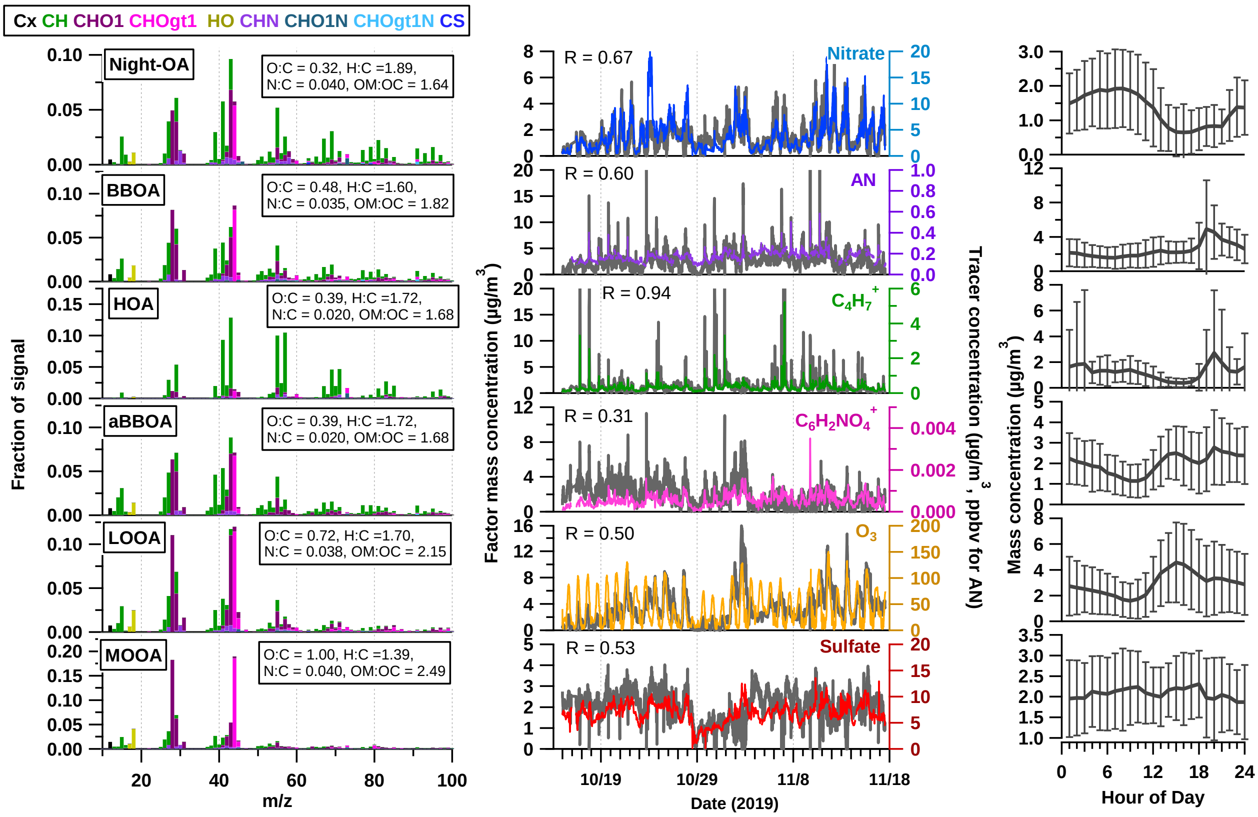

Figure S2. (a) Mass spectral profile in family groups and (b) time series of PMF OA components. Also exhibited are concentration variations of tracer compounds on the right axes.

afternoon-peak, aBBOA factor was attributed to the quick aging process of biomass burning emissions. Note that gaseous pollutants could also be released during biomass burning and then be oxidized to form organic aerosols. As shown in Fig.S2, the aBBOA factor is positively correlated with $C_6H_2NO_4^+$ (m/z 151.998, R =0.31), which is a typical fragment of the aged BBOA component nitrocatechol (Bertrand *et al.*, 2018). Therefore, we speculate this factor was related to the aged biomass burning emissions. In Heshan site, a night-formed OA factor (Night-OA) was resolved with a pronounced evening elevation in the diurnal circle. Night-OA is correlated with nitrate (R = 0.67) which was likely associated with NO_3 nighttime chemistry as discussed previously (Kuang *et al.*, 2021).

1.2 The modelling method of $\boldsymbol{AAE_{BC,\lambda-880}}$

The absorption coefficient $\sigma_{abs,Mie,\lambda}$ was obtained by the following:

$$\sigma_{abs,Mie,\lambda} = \int Q_{abs,Mie,\lambda}(Dp) * \left(\frac{\pi}{4} D_p^2\right) N\left(logD_p\right) * d_{logD_p} \text{ (1)}$$

where $N\left(logD_p\right)$ is the PNSD function, $Q_{abs,Mie,\lambda}$ is absorption efficiency which is simulated using the Mie-theory, D_p is the particle. For D_p bin, particles are classified into three types: non-light-absorbing particles (Non-BC), BC-containing particles and pure BC particles. Parameters r_{ext} defined as mass fraction of pure externally mixed BC (M_{ext}) to total BC mass (M_{BC}) in different diameter bins and R_NBC defined as the number fraction of particles that does not contain BC are used to represent BC mixing state. The PNSD of Non-BC particles ($N(logD_p)_{Non-BC}$) and BC-containing particles ($N(logD_p)_{BC}$) can be given by the following equations:

$$N(logD_p)_{Non-BC} = N(logD_p)_{measure} * R\_NBC \text{ (2)}$$

$$N(logD_p)_{BC} = N(logD_p)_{measure} * (1 - R\_NBC) \text{ (3)}$$

Where R_NBC is the number fraction of BC-free particles, $N(logD_p)_{measure}$ is the PNSD measured by the SMPS and APS. The PNSD of pure BC particles ($N(logD_p)_{ext}$) and core–shell mixed BC particles ($N(logD_p)_{core-shell}$) can be given by the following equations:

$$r_{ext} = \frac{M_{ext}}{M_{BC}} \text{ (4)}$$

$$N(logD_p)_{ext} = N(logD_p)_{BC} * f_{ext}(Dp) \text{ (5)}$$

$$N(logD_p)_{core-shell} = N(logD_p)_{BC} * (1 - f_{ext}(Dp) \text{ (6)}$$

$f_{ext}(Dp)$ is volume fraction of pure BC at each diameter bin which can be calculated by :

$$f_{ext}(Dp) = \frac{M_{BC}(Dp) * r_{ext}}{\rho_{BC} * N(logD_p)_{BC} * (\frac{\pi}{6} D_p^3)} \text{(7)}$$

where ρ_{BC} is the density of BC (1.5 g cm^{-3})(Ma *et al.*, 2012); M_{BC} is derived from AE33. Size distribution of BC mass $M_{BC}(Dp)$ is calculated based on the normalized Cx fraction $f_{Cx}(Dp)$ at each diameter bin:

$$M_{BC}(Dp) = M_{BC} \times f_{Cx}(Dp) \text{ (8)}$$

In addition to the PNSD of the three types of particles mentioned above, another key parameter of the core-shell model is the diameter of the BC core, at each diameter bin the D_{core} is calculated as:

$$D_{core} = \left(\frac{6 \times M_{BC}(Dp) * (1 - r_{ext})}{\rho_{BC} * \pi}\right)^{1/3} \text{ (9)}$$

After obtaining the absorption coefficient at each wavelength, the AAE at two wavelengths is calculated as the following equation:

$$\mathrm{AAE}_{\lambda1-\lambda2} = \frac{\ln(\sigma_{\mathrm{abs},\lambda1}) - \ln(\sigma_{\mathrm{abs},\lambda2})}{\ln(\lambda_1) - \ln(\lambda_2)} \quad (10)$$

When retrieving BrC absorptions, calculations of $\mathrm{R}_{\mathrm{AAE}}(\lambda)$ were achieved through assuming $\mathrm{r}_{\mathrm{ext}}$ and R_NBC values of 0.5 and 0.5 due to small influences of $\mathrm{r}_{\mathrm{ext}}$ and R_NBC variations on $\mathrm{R}_{\mathrm{AAE}}(\lambda)$.

1.3 Mass Scattering Efficiency calculations for different aerosol components.

The size distributions of ammonium (AN) nitrate and ammonium sulfate (AS) paired from measured size distributions of nitrate, ammonium and sulfate by the SP-AMS under different non-refractory mass concentrations of PM_1 ($\mathrm{NR\_PM}_1$, PM_1 corresponds to aerosols with aerodynamic diameter less than 1 μm) is shown in Fig.S3a and Fig.S3b. Note that the D_m converted by assuming an aerosol density of 1.6 g/cm^3 from the SP-AMS vacuum aerodynamic diameter Dva. The $\mathrm{MSE}_{\mathrm{AN,PM1}}$ defined as $MSE_{PM1} = \frac{\sigma_{sp,PM1}}{AN_{PM1}}$ under different $\mathrm{NR\_PM}_1$ conditions and results of $\mathrm{MSE}_{\mathrm{AS,PM1}}$ are shown in Fig.S3c. The density of AS and AN are 1.769 and 1.72 g/cm^3, and used refractive index of AS and AN is 1.53-10^{-7}i. However, in this study, the aerosol scattering coefficient of PM_{10} (aerosols with aerodynamic diameter less than 10 μm) and the aerosol mass concentration of PM_1 is measured by the SP-AMS. Therefore, the corrected MSE defined as $MSE_{Corrected} = \frac{\sigma_{sp,PM10}}{AN_{PM1}} = MSE_{PM1} \times C$ is simulated and also shown in Fig.S3c, and C is the correction factor. The average $MSE_{Corrected}$ values for AS and AN are 4.6 and 4.8 m^2/g, and used in this study.

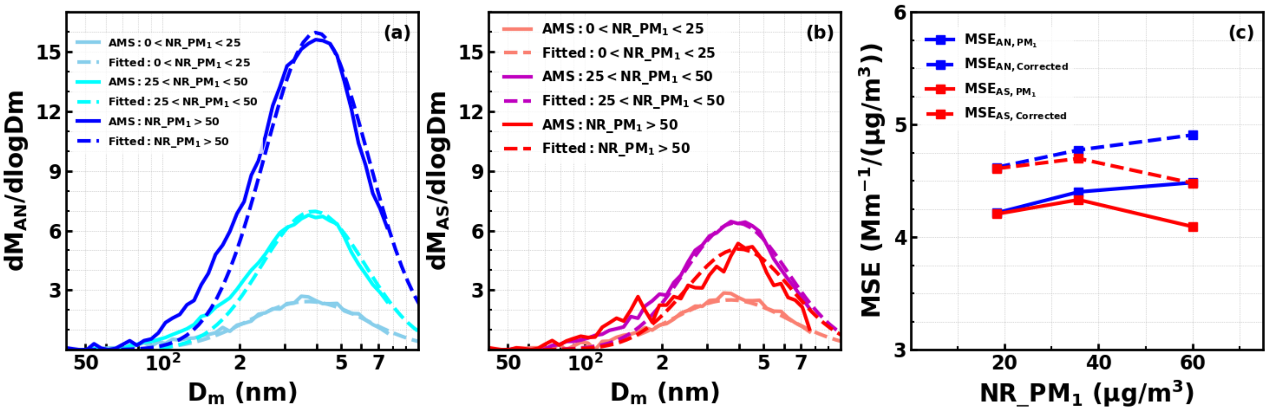

Figure S3. Average size distributions of AN **(a)** and AS **(b)** under different NR_PM1 conditions, solid lines are measurement averages of SP-AMS measurements and dashed lines are corresponding lognormal fitting curves; **(c)** Simulated PM1 MSE of AS and AN under different NR_PM1 conditions and corrected ones

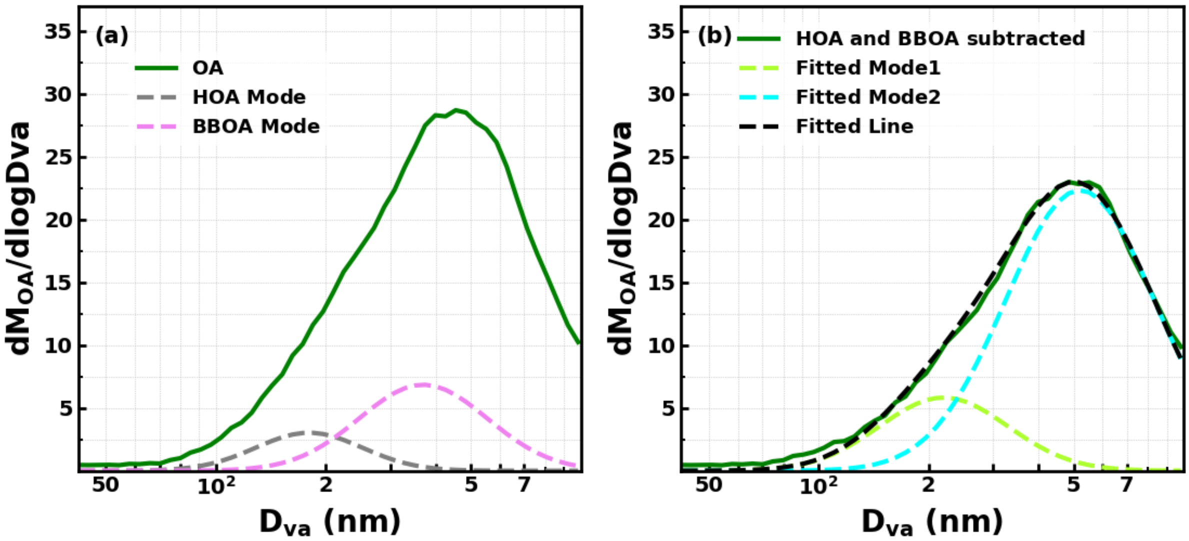

Figure S4. **(a)** Average OA size distributions, and parts associated with HOA and BBOA, Dva is the vacuum aerodynamic diameter. **(b)** The average OA size distributions with contributions of HOA and BBOA subtracted, and the remaining can be well fitted using two lognormal modes.

The MSE_{HOA} is simulated on the basis of identified average HOA D_{gv} and σ_g of 180 nm and 1.46 using the Mie theory in combination with calculated HOA density of 1.15 g/cm3. The calculated MSE_{HOA} is 3.2 m^2/g. The MSE_{BC} is simulated using the normalized Cx distribution shape shown in Fig.s4, and assuming an BC density of 1.5 g/cm3 and BC refractive index of 1.8-0.54i. The calculated MSE_{BC} is 2.8 m^2/g.

The average size distributions of OA measured by the SP-AMS during the entire campaign is shown in Fig.S4a. The average size distributions of HOA and BBOA calculated from average HOA and BBOA mass concentrations together with identified average Dgv and σ_g of HOA and BBOA identified from SP-AMS measurements (175, 395 and 1.46, 1.55 for HOA and BBOA) are also shown in Fig.S4a. If the contributions of HOA and BBOA are subtracted (Fig.S2b), the OA size distribution can be well fitted using two lognormal modes. The mass concentration of fitted Mode 1 is consistent that of aBBOA and obviously different with mass concentrations of other remaining OA factors, and mass concentration of fitted Mode 2 is consistent with the sum of LOOA, MOOA and Night-OA. Thus, the Mode 1 is identified as the size distribution of aBBOA. The Mode 2 of LOOA， MOOA and Night-OA suggests that most secondary organic aerosols during this campaign are likely internally mixed. Thus the MSE_{aBBOA} is simulated as 4.5 m2/g with identified size distribution of Mode 1 and calculated aBBOA density g/cm3 using the scheme proposed by (Kuwata *et al.*, 2012). Corrected MSE of MOOA, Night-OA, LOOA (MSE_{SOA}) is calculated as 6.3 m2/g with identified size distribution of Mode 2 and estimated average density of 1.31 g/cm3 using volume weighting rule.

1.4 Refractive index retrieval

Determined BBOA MSEs and MAEs were converted to Volume scattering or absorption efficiency (VSE or VAE) through VSE=MSE*density. With given geometric mean (Dgn) and standard deviation (σg) values of the PNSD. The assuming total number concentration of 1000 (Ntot=1000 /cm3), PNSD can be given as :

$$N(logDp) = \frac{dN}{dlogDp}(Dp) = \frac{\mathrm{Ntot}}{\sqrt{2\pi}\,\log(\sigma_g)}\exp\left[-\frac{(\log(D_p)-\log(D_{gn}))^2}{2\log^2\sigma_g}\right] \quad (11)$$

The with given refractive index of $m=m_{R,BBOA}+m_{i,BBOA}\times i$, the aerosol scattering efficiency Q_{sca} and absorption efficiency Q_{abs} can be calculated using the Mie theory. And then scattering and absorption coefficients of bulk aerosols can be derived as:

$$\sigma_{sca}(\lambda) = \int_0^{D_p^{max}} Q_{sca}(m,\lambda,D_p) \times \frac{\pi}{4} D_p^2 \times N(logD_p) \times dlogD_p \quad (12)$$

$$\sigma_{abs}(\lambda) = \int_0^{D_p^{max}} Q_{abs}(m,\lambda,D_p) \times \frac{\pi}{4} D_p^2 \times N(logD_p) \times dlogD_p \quad (13)$$

Where λ is the optical wavelength, and D_p^{max} of 2500 nm is set. The total volume concentration can be calculated as:

$$Vtot = \int_0^{D_p^{max}} \frac{\pi}{6} D_p^3 \times N(logD_p) \times dlogD_p \quad (14)$$

Then the VSE and MAE can be calculated as:

$$VSE(\lambda) = \frac{\sigma_{sca}(\lambda)}{Vtot} \quad (15)$$

$$VAE(\lambda) = \frac{\sigma_{abs}(\lambda)}{Vtot} \quad (16)$$

The $m_{R,BBOA}$ was retrieved through varying $m_{R,BBOA}$ in iterations to find a $m_{R,BBOA}$ with which the derived VSE can be reproduced, in these iterations $m_{i,BBOA}$ was parameterized with the corresponding ΔCO/ΔBBOA using the relationships determined in Sect.3.4. The $m_{i,BBOA}$ was retrieved through varying $m_{i,BBOA}$ in iterations to find a $m_{R,BBOA}$ with which the derived VAE can be reproduced, and $m_{R,BBOA}$ are fixed as 1.6 due to that sensitivity tests show that very small influences of $m_{R,BBOA}$ variations on $m_{i,BBOA}$ retrieval.

2. Other figures

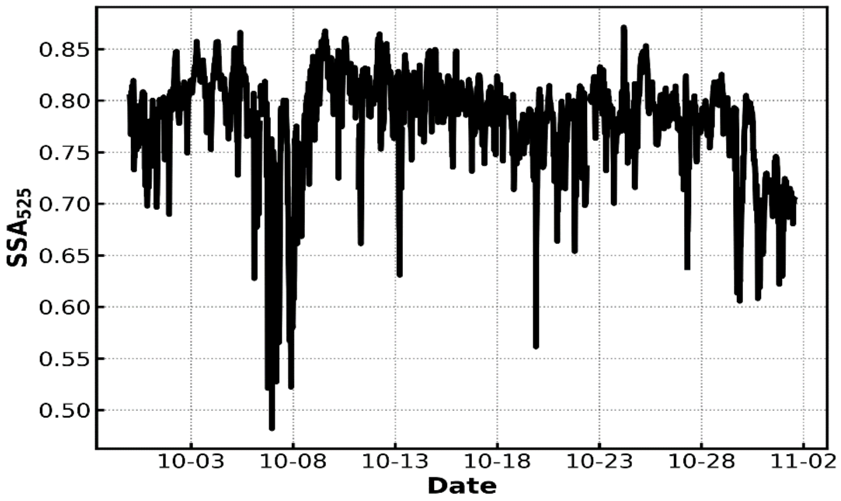

Figure S5. Time series of SSA during the campaign.

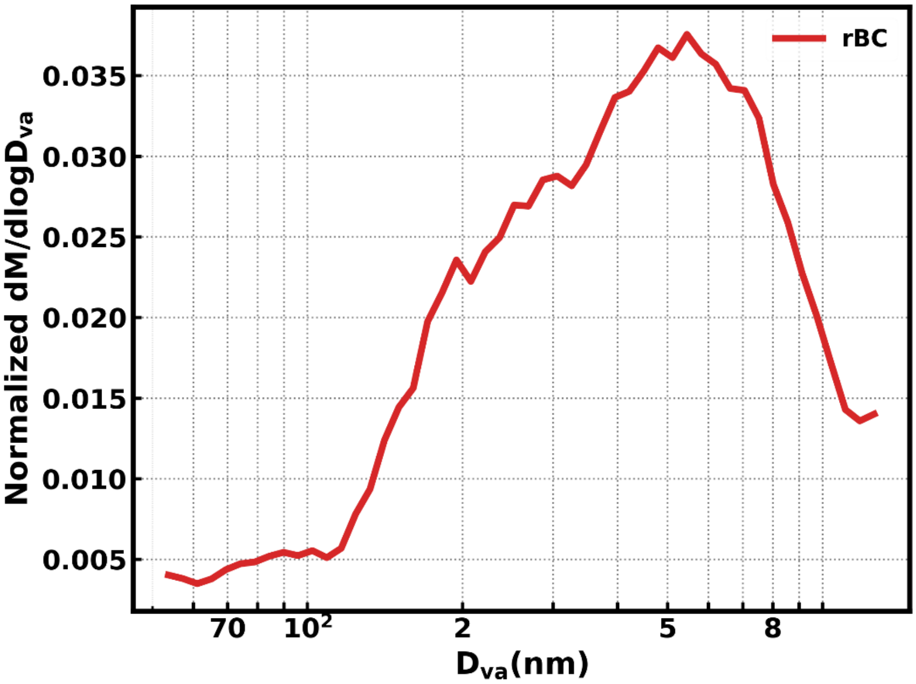

Figure S6. Normalized average Cx distribution measured by the SP-AMS.

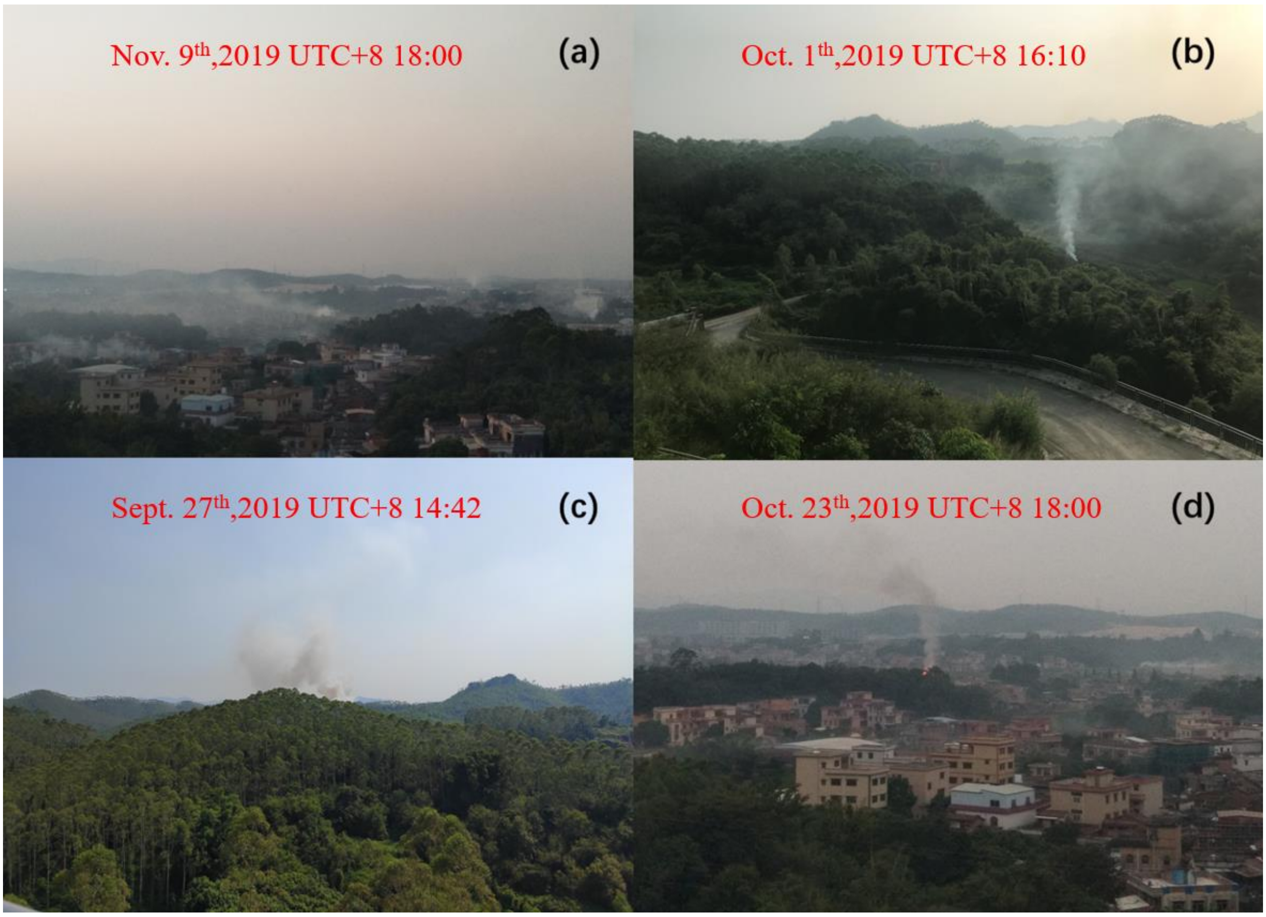

Figure S7. Photoed at at the Heshan supersite during the observation period.

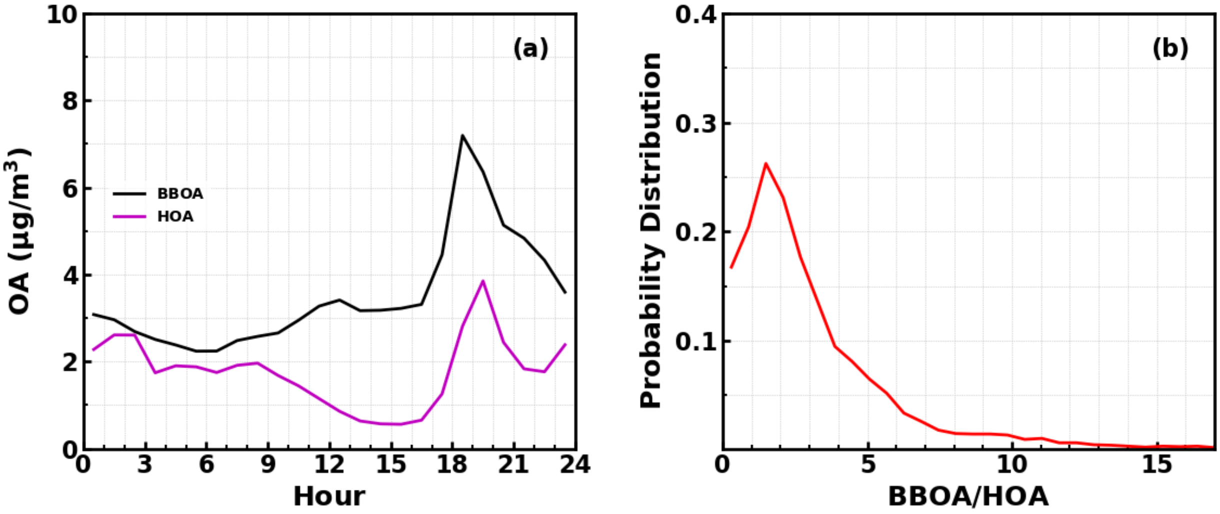

Figure S8. **(a)** Diurnal variations of BBOA and HOA; **(b)** The distribution of BBOA/HOA ratio.

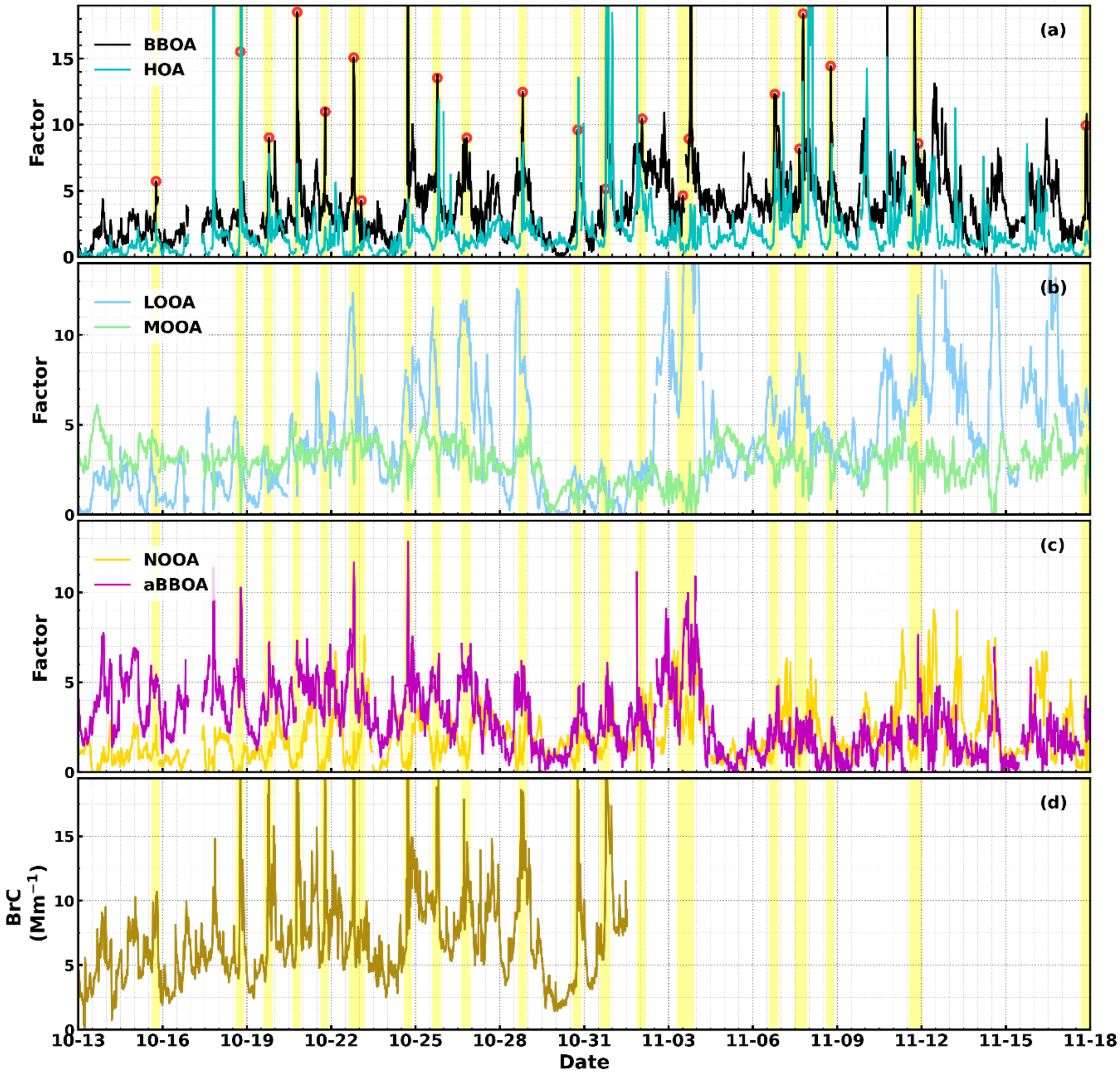

Figure S9. **(a)** to **(c)** Time series of resolved OA factors by SP-AMS measurements, and **(d)** is the derived BrC absorption coefficients at 370 nm. Shaded areas represent identified spikes.

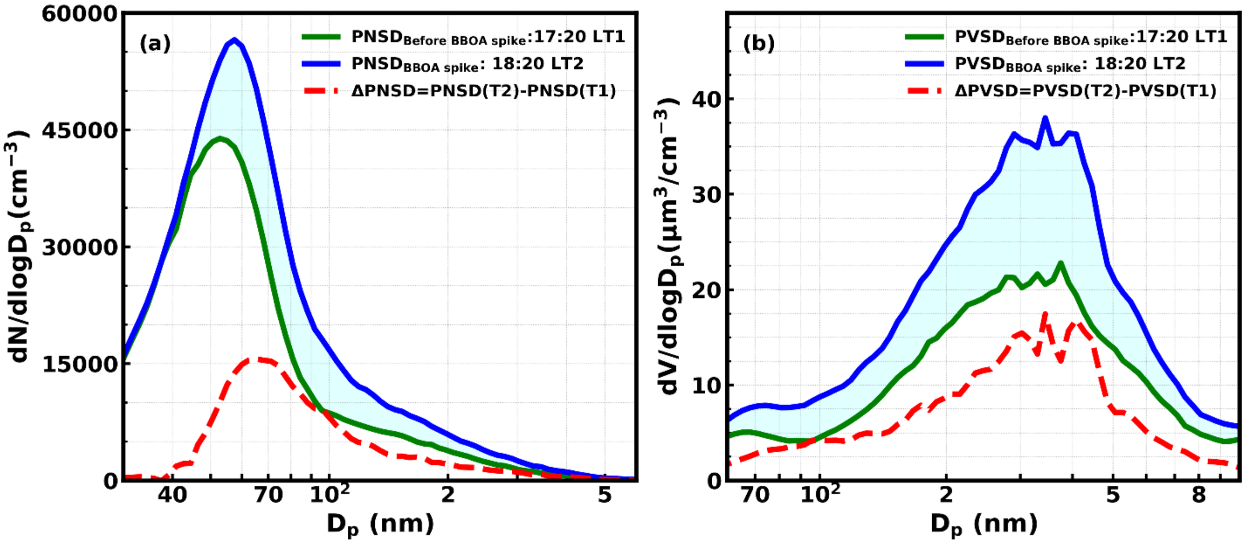

Figure S10. Examples of identifying differences of PNSD (△PNSD) and PVSD (△PVSD)

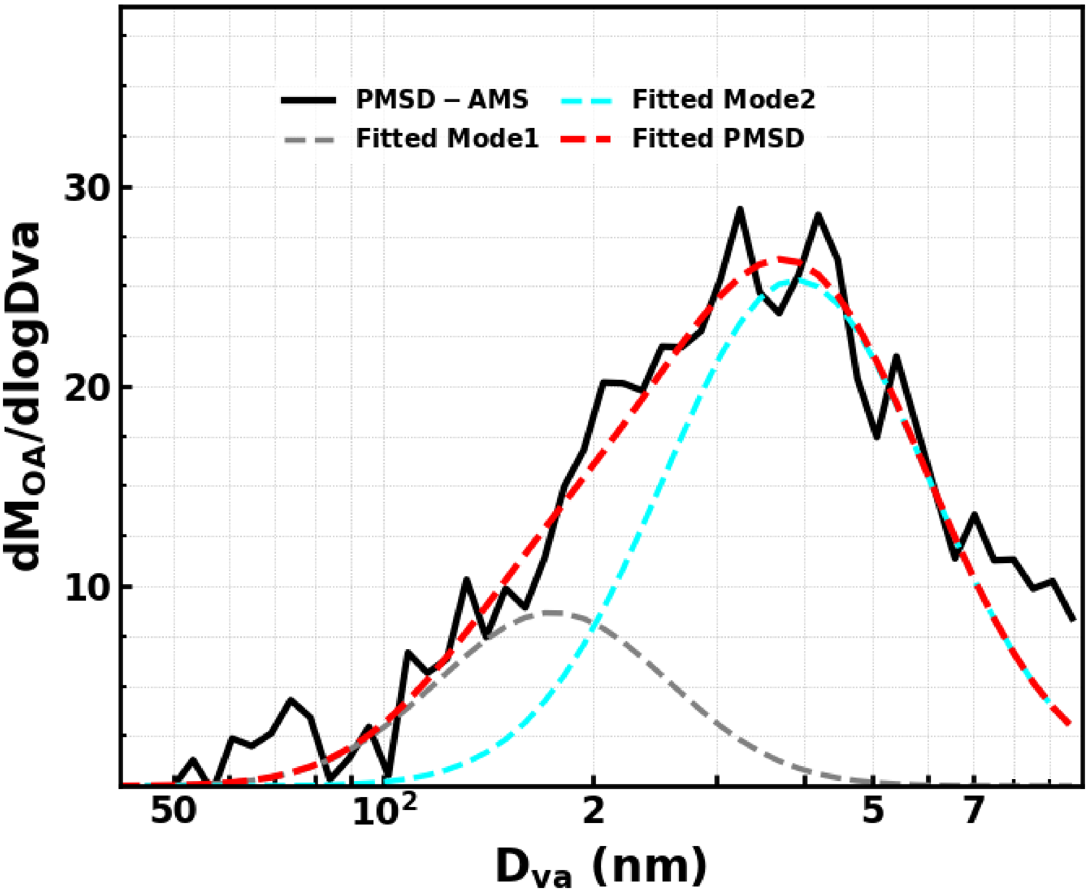

Figure S11. Average OA size distribution differences for spikes in Fig.3b, and the difference can be fitted using two lognormal modes, corresponding to HOA and BBOA respectively.

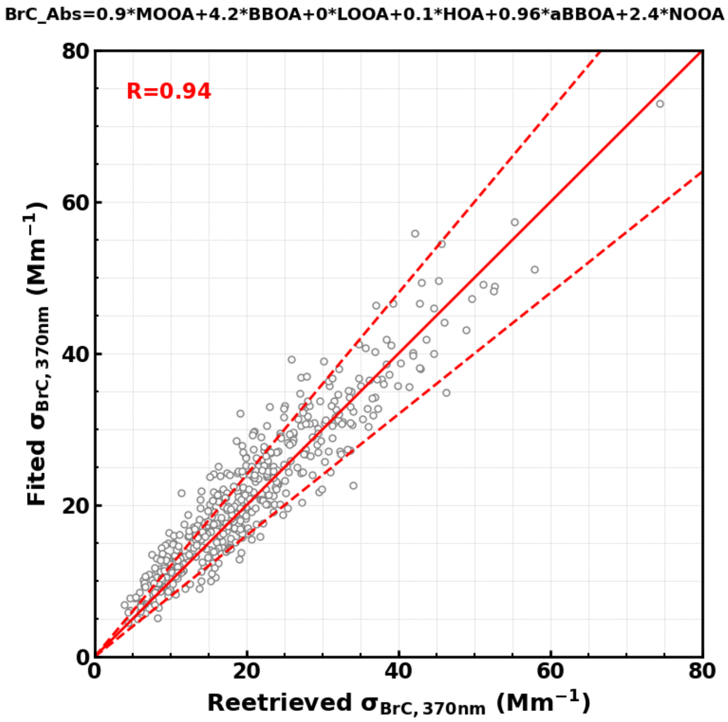

Figure S12. Multilinear fitting of BrC absorptions at 370 nm with OA factors

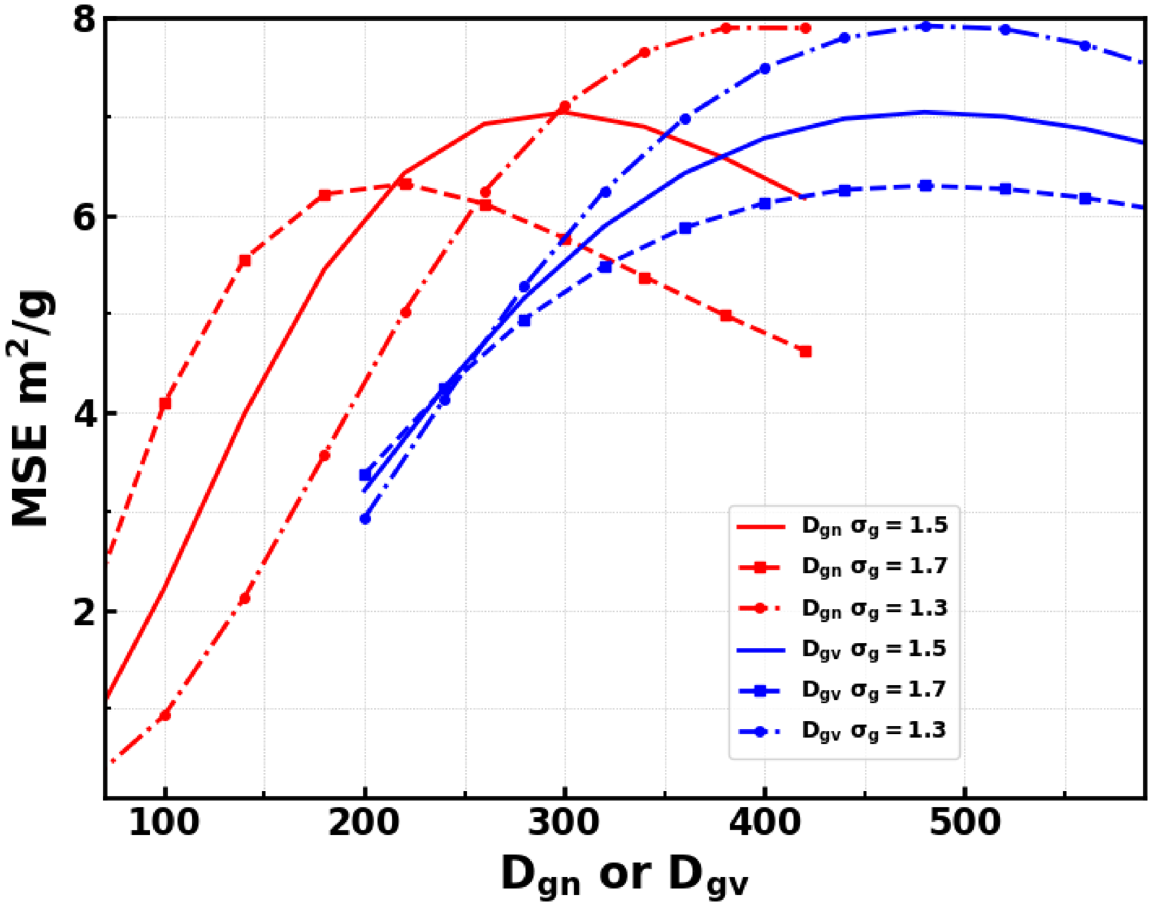

Figure S13. Variations of BBOA MSE under different Dgv, Dgn and σ_g conditions.

References

Bertrand A., Stefenelli G., Jen C. N., Pieber S. M., Bruns E. A., Ni H., Temime-Roussel B., Slowik J. G., Goldstein A. H., El Haddad I., Baltensperger U., Prévôt A. S. H., Wortham H., and Marchand N. (2018), Evolution of the chemical fingerprint of biomass burning organic aerosol during aging, *Atmos. Chem. Phys.*, *18*(10), 7607-7624, doi:10.5194/acp-18-7607-2018.

Huang S., Wu Z., Poulain L., van Pinxteren M., Merkel M., Assmann D., Herrmann H., and Wiedensohler A. (2018), Source apportionment of the organic aerosol over the Atlantic Ocean from 53°N to 53°S: significant contributions from marine emissions and long-range transport, *Atmos. Chem. Phys.*, *18*(24), 18043-18062, doi:10.5194/acp-18-18043-2018.

Kuang Y., Huang S., Xue B., Luo B., Song Q., Chen W., Hu W., Li W., Zhao P., Cai M., Peng Y., Qi J., Li T., Wang S., Chen D., Yue D., Yuan B., and Shao M. (2021), Contrasting effects of secondary organic aerosol formations on organic aerosol hygroscopicity, *Atmos. Chem. Phys.*, *21*(13), 10375-10391, doi:10.5194/acp-21-10375-2021.

Kuwata M., Zorn S. R., and Martin S. T. (2012), Using Elemental Ratios to Predict the Density of Organic Material Composed of Carbon, Hydrogen, and Oxygen, *Environmental science & technology*, *46*(2), 787-794, doi:10.1021/es202525q.

Lanz V. A., Alfarra M. R., Baltensperger U., Buchmann B., Hueglin C., and Prévôt A. S. H. (2007), Source apportionment of submicron organic aerosols at an urban site by factor analytical modelling of aerosol mass spectra, *Atmos. Chem. Phys.*, *7*(6), 1503-1522, doi:10.5194/acp-7-1503-2007.

Ma N., Zhao C. S., Müller T., Cheng Y. F., Liu P. F., Deng Z. Z., Xu W. Y., Ran L., Nekat B., van Pinxteren D., Gnauk T., Müller K., Herrmann H., Yan P., Zhou X. J., and Wiedensohler A. (2012), A new method to determine the mixing state of light absorbing carbonaceous using the measured aerosol optical properties and number size distributions, *Atmos. Chem. Phys.*, *12*(5), 2381-2397, doi:10.5194/acp-12-2381-2012.

Ng N. L., Canagaratna M. R., Jimenez J. L., Zhang Q., Ulbrich I. M., and Worsnop D. R. (2011), Real-Time Methods for Estimating Organic Component Mass Concentrations from Aerosol Mass Spectrometer Data, *Environ. Sci. Technol.*, *45*(3), 910-916, doi:10.1021/es102951k.

Paatero P. (1997), Least squares formulation of robust non-negative factor analysis, *Chemometr Intell Lab*, *37*(1), 23-35, doi:10.1016/S0169-7439(96)00044-5.

Paatero P., and Tapper U. (1994), Positive matrix factorization: A non-negative factor model with optimal utilization of error estimates of data values, *Environmetrics*, *5*(2), 111-126, doi:10.1002/env.3170050203.

Sun Y. L., Zhang Q., Schwab J. J., Yang T., Ng N. L., and Demerjian K. L. (2012), Factor analysis of combined organic and inorganic aerosol mass spectra from high resolution aerosol mass spectrometer measurements, *Atmos. Chem. Phys.*, *12*(18), 8537-8551, doi:10.5194/acp-12-8537-2012.

Ulbrich I. M., Canagaratna M. R., Zhang Q., Worsnop D. R., and Jimenez J. L. (2009), Interpretation of organic components from Positive Matrix Factorization of aerosol mass spectrometric data, *Atmos. Chem. Phys.*, *9*(9), 2891-2918, doi:10.5194/acp-9-2891-2009.